ORIGINAL PAPER

Synthesis, substitution kinetics, DNA/BSA binding and cytotoxicity of tridentate N^E^N (E = NH, O, S) pyrazolyl palladium(II) complexes

Reinner O. Omondi[1,2] · Adewale O. Fadaka[3,4] · Amos A. Fatokun[5] · Deogratius Jaganyi[6,7] · Stephen O. Ojwach[1]

Abstract

The pincer complexes, [Pd(**L₁**)Cl]BF₄ (**PdL₁**), [Pd(**L₂**)Cl]BF₄ (**PdL₂**), [Pd(**L₃**)Cl]BF₄ (**PdL₃**), [Pd(**L₄**)Cl]BF₄ (**PdL₄**) were prepared by reacting the corresponding ligands, 2,6-bis[(1H-pyrazol-1-yl)methyl]pyridine (**L₁**), bis[2-(1H-pyrazol-1-yl)ethyl] amine (**L₂**), bis[2-(1H-pyrazol-1-yl)ethyl]ether (**L₃**), and bis[2-(1H-prazol-1-yl)ethyl]sulphide (**L₄**) with [PdCl₂(NCMe)]₂ in the presence NaBF₄. The solid-state structures of complexes **PdL₁**–**PdL₄** confirmed a tridentate coordination mode, with one chloro ligand completing the coordination sphere to afford square-planar complexes. Chemical behaviour of the complexes in solution confirms their stability in both aqueous and DMSO stock media. The electrochemical properties of the compounds showed irreversible two-electron reduction process. Kinetic reactivity of Pd complexes with the biological nucleophiles viz, thiourea (**Tu**), L-methionine (**L-Met**) and guanosine 5′-diphosphate disodium salt (**5'-GMP**) followed the order: **PdL₂** < **PdL₃** < **PdL₄**, and **PdL₂** < **PdL₁**. The kinetic reactivity is subject to the electronic effects of the spectator ligand(s), and the trend was supported by the DFT computed results. The palladium complexes **PdL₁**–**PdL₄** bind to calf thymus (CT-DNA) via intercalation mode. In addition, the bovine serum albumin (BSA) showed good binding affinity to the complexes. The mode of quenching mechanism of the intrinsic fluorescence of CT-DNA and BSA by the complexes was found to be static. The order of interactions of the complexes with DNA and BSA was in tandem with the rate of substitution kinetics. The complexes, however, displayed relatively low cytotoxicity (IC₅₀ > 100 μM) when tested against the human cervical adenocarcinoma (HeLa) cell line and the transformed human lung fibroblast cell line (MRC-5 SV2).

Graphical abstract
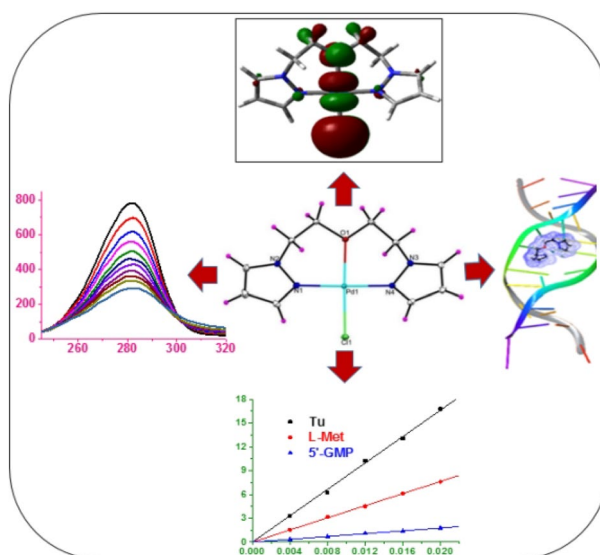
Extended author information available on the last page of the article

Introduction

There has been a growing interest in expanding the anticancer activity of metallo-compounds besides Pt-drugs. Among the non-Pt-drugs, Pd(II) complexes have become promising alternatives by displaying better anti-proliferative properties and favourable toxicity profile [1–4]. Pd(II) complexes have been viewed as suitable anticancer drug candidates due their noticeable enzymatic catalytic attributes and ability to cleave the double structure of DNA [3]. An essential characteristic of Pd-containing chemotherapy drugs is their lower kidney toxicity than cisplatin [5]. Also, a positive correlation is observed between the solubility of Pd(II) complexes and their cytotoxic effects [6, 7]. However, the main challenge for the development of antitumour Pd(II) complexes is their high hydrolysis and reactivities (10^5 times faster than Pt), resulting in the formation of multiple reactive species that are unable to reach the pharmacological target [5]. Consequently, the selection of suitable carrier ligands to regulate the reactivity and stability of Pd(II) compounds is one of the foremost challenges in the design and development of Pd(II)-antitumour drugs [5]. Pincer-type spectator ligands have become increasingly popular in the development of stable Pd(II)-based anticancer drugs in the presence of biological thiols [8–10], owing to their ability to stabilise the metal centres more effectively than their related mono and bidentate variants.

Pincer ligands have been shown to be relatively non-toxic, and their versatile structures can easily be fine-tuned to ensure desirable properties and reactivity, as in solubility and cytotoxic [8]. For example, Bugarčić [11–14] and Jaganyi [15, 16] laboratories have examined the nucleophilic substitution reactions of Pd(II) complexes of pincer ligands with nitrogen donor atoms. The findings of the studies depict that π-acceptor and π/σ-donor has an essential role in determining the reactivity of the compounds. In another study, Ćoćić and the group [17] used pincer-type ligands to control the kinetic reactivity of Pd(II) complexes, thus improving their resultant cytotoxicity. The work revealed that steric crowding reduces the lability of the leaving groups, DNA/BSA binding properties and cytotoxic effects of Pd(II) compounds. In another study, Pd(II) complexes supported by N-heterocyclic ligands were found to be stable in aqueous solutions containing physiological thiols [10]. The NHC moiety stabilises the Pd(II) centres, due to its strong sigma-donating ability. These Pd(II) complexes demonstrated in vitro cytotoxicity against cancer cells, in vitro angiogenesis and in vivo cytotoxic effects on tumour xenografts

in nude mice model, with no noticeable toxicity [8]. The mechanism of action of the complexes was found to involve induction of mitochondrial dysfunction and inhibition of EGFR signalling pathway.

In our recent contribution [18], we carried out a systematic investigation of the electronegative effects on the rate of kinetic reactivity of Pd(II) complexes using heteroatoms positioned remotely on the spectator ligand(s) backbone, and thereby enhancing DNA binding propensity and the resultant cytotoxic effects. Overall, Pd(II) complexes with high kinetic lability in the study demonstrated the highest DNA binding affinities, and improved cytotoxic activities on the studied tumour cell lines. Inspired by these findings, the present study focuses on the competing roles of *trans*-heteroatoms on carrier ligands typified by N^E^N donor atom (where E = NH, O, S) on kinetic reactivity and the biological activities of Pd(II) complexes. We report in detail the synthesis, structural characterisation, ligand substitution reactions, DNA and BSA protein interactions and cytotoxic activities of the complexes against the human cervical adenocarcinoma (HeLa) cell line and the transformed human lung fibroblast (MRC-5 SV2) cell line. The rates of kinetics reactivity were evaluated using biological nucleophiles: thiourea (**Tu**), L-methionine (**L-Met**) and guanosine-5'-monophosphate (**5'-GMP**). The interaction mechanisms of the Pd(II) complexes with DNA/protein molecules at the atomic level were rationalised by in silico approach and are herein described.

Results and discussion

Preparation and characterisation of ligands and their respective Pd(II) complexes

The bis-(pyrazolyl) ligands used in the study were synthesised in good yields via phase transfer catalysed (PTC) alkylation of pyrazole using 2,6-bis(chloromethyl)pyridine (**L₁**), bis(2-chloroethyl)amine (**L₂**), bis(2-chlroethyl)ether (**L₃**), and (2-chloroethyl)-1H-pyrazole (**L₄**), following previously reported literature procedures [19–21] (Scheme 1), and their spectroscopic data are recorded in the supplementary information). Subsequent treatment of equimolar amounts of **L₁**–**L₄** and [PdCl₂(NCCH₃)₂], with NaBF₄ as a counter ion in CH₂Cl₂ gave the corresponding complexes **PdL₁**–**PdL₄**, respectively, with yield of 60–85% (Scheme 1).

The purity and structures of **PdL₁**–**PdL₄** were established using ^{1}H and ^{13}C NMR (Figs. S1–S13) and FT-IR (Figs.

Scheme 1 Synthetic pathways of tridentate pyrazol-1-yl ligands (NH, S, and O pincer type) and their respective Pd(II) complexes. **a** 40% NaOH, 40% TBAB, toluene, 18 h; **b** NaH, Dry DMF, 60 °C, 30 h; **c** PdCl$_2$(NCCH$_3$)$_2$, CH$_2$Cl$_2$, NaBF$_4$, 12 h; **d** Na$_2$S.9H$_2$O, NaOH, H$_2$O/Et$_2$OH
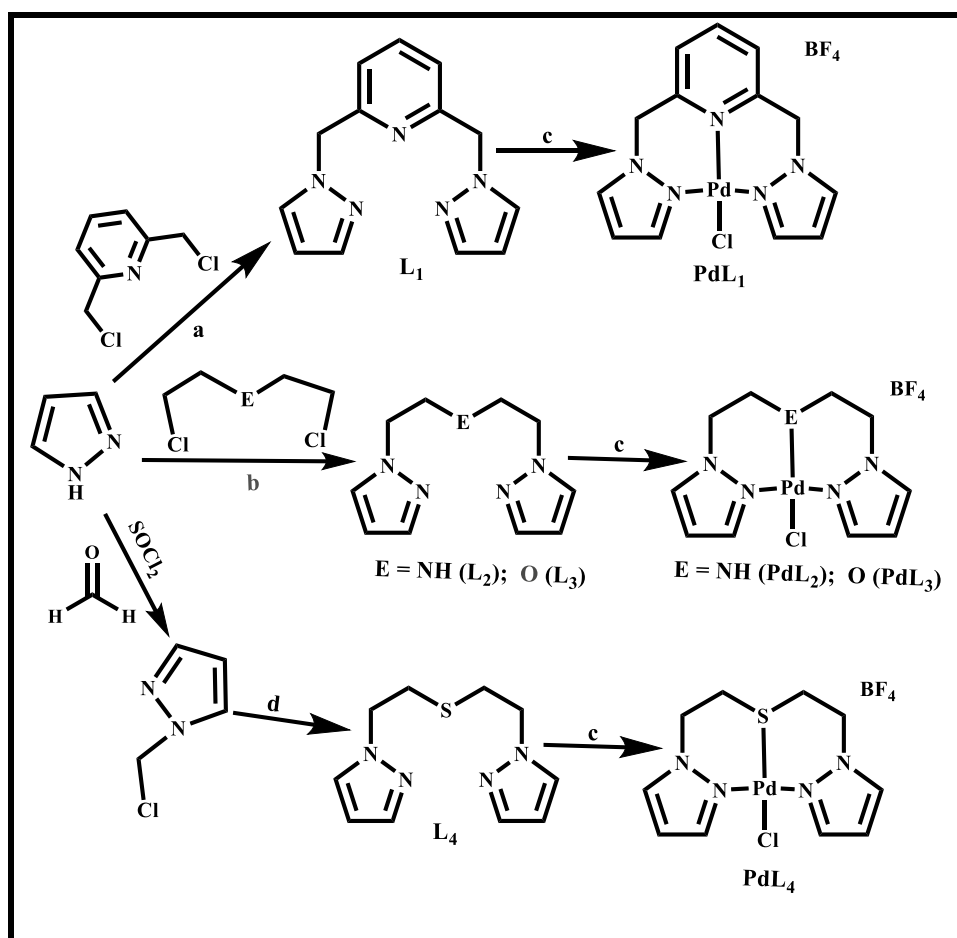
S14–S22), LC–MS (Figs. S23–S30), elemental, and X-ray structural analyses. As an illustration, ^{1}H NMR spectrum of ligand **L$_4$** showed two distinct triplets for the CH$_2$ protons, compared to four sets of signals for the CH$_2$ linker protons in the respective complex **PdL$_4$** (Fig. S9). The appearance of the four sets of methylene signals in **PdL$_4$** is attributed to the increased restricted rotations (structural rigidity) arising from the occurrence of stable chair and twist-boat (skew-boat) conformations in the complex in relation to the more fluxional molecular behaviour or dynamic exchange process (unrestricted rotation) in the ligand [21]. The ^{1}H NMR spectra of the remaining ligands **L$_1$–L$_3$** and their respective complexes **PdL$_1$–PdL$_3$** are shown in Figs. S1–S8.

Also, from the ^{13}C NMR, the downfield shifts of the resonance of methylene carbon at 31.18 and 51.05 ppm (**L$_4$**) to 36.14 and 52.31 ppm (**PdL$_4$**), Fig. S13, are in tandem with formation of the complex (^{13}C NMR spectra of the other compounds are given in Figs. S10–S12). FT-IR spectroscopy was also adopted in the determination of the identity of the ligands and their corresponding complexes (**Fig. S14–S22**). For example, a considerable shift of the absorption bands of C=N from 1395 cm^{-1} (**L$_4$**) to higher frequency of 1415 cm^{-1} (**PdL$_4$**) suggests the coordination of the Pd(II)

ion to the N-atoms of the pyrazolyl units. Similarly, an upfield shift of the C–S wavenumber from 748 cm^{-1} (**L$_4$**) to 776 cm^{-1} (**PdL$_4$**) is also consistent with the formation of the complexes (Fig. S22). A shift of the absorption bands to higher frequencies upon coordination indicates the sigma donor property of the spectator ligand(s) [22]. The identities of the compounds were also confirmed by LC–MS technique, and all complexes gave the anticipated molecular ion peak (M$^+$). For instance, the expanded ESI mass spectrum of complex **PdL$_4$** with *m/z* at 362 (64%) corresponds to the exact mass of 362.97, Fig. S30a. The observed mass spectra were consistent with the calculated isotopic mass distributions of the complexes (Figs. S27–S230). The experimental values of elemental analyses of complexes **PdL$_1$–PdL$_4$** comply with the suggested molecular structures indicated in Scheme 1; the values also confirm the purity of the bulk materials.

X-ray structural analysis of complexes PdL$_1$–PdL$_4$.

Suitable single crystals of **PdL$_1$–PdL$_4$** for X-ray diffraction measurements were afforded by slow evaporations of concentrated CH$_2$Cl$_2$/Et$_2$O solutions at 25 °C. ORTEP

representations of the molecular structures of **PdL₁–PdL₄** are shown in Fig. 1. The crystallographic data for the complexes are summarised in Tables S1 and S2, respectively.

As shown in Fig. 1, the solid-state structures of **PdL₁–PdL₄** reveal four-coordinate complexes in distorted square-planar geometries. The six-membered ring, $N(1)–Pd(1)–N_{pyridine}$, of 89.81(8) ° (**PdL₁**), is smaller than $N(1)–Pd(1)–NH$ of 93.5(3) ° (**PdL₂**), and $N(1)–Pd(1)–O$ of 90.98(5)° (**PdL₃**), a characteristic of the greater constraint imposed by the restricted rotations of the pyridine ring (**PdL₁**) than the more flexible CH_2 linkers (**PdL₂** and **PdL₃**). The longer bond distance Pd(1)–Cl(1) of 2.3149(6) (**PdL₄**) in comparison to Pd(1)–Cl(1), 2.293(2) (**PdL₂**) and Pd(1)–Cl(1), 2.2574(4) (**PdL₃**) is due to the stronger *trans*-influence of S atom (soft ligating atom) than N_{imid} and O atom (which are hard bases). Also, the observed longer Pd(1)–Cl(1) of **PdL₂** in relation to **PdL₃** is ascribed the higher polarizability of NH than O atom, resulting in a stronger σ-bonding to Pd-metal centre (increasing *trans*-labilisation effect). The shorter bond lengths of Pd(1)–Cl(1) of 2.2793(6) Å (**PdL₁**) than Pd(1)–Cl(1) of 2.293(2) Å (**PdL₂**) is attributable to better *trans*-influence of NH specie (σ-donor) than the pyridine moiety (π-acceptor). The Pd(1)–Cl(1) bond distance of 2.2793(6) (**PdL₁**) compares well with the average of 2.289 ± 0.013 Å for 20 similar

structures [23]. With the exception of Pd(1)–Cl(1) bond distances 2.2574(4) Å for **PdL₃** (lower than the minimum value 2.281 Å), Pd(1)–Cl(1) bond distances of 2.293(2) and 2.3149(6) for **PdL₂** and **PdL₄**, respectively, correlate well with the mean of 2.308 ± 0.020 Å obtained for 25 related structures [24].

Stability of complexes PdL₁–PdL₄ in aqueous buffer and dimethyl sulfoxide (DMSO) solutions

The stability tests of **PdL₁–PdL₄** in aqueous (50 μM Tris buffer containing 50 mM NaCl, pH 7.2) and DMSO media were conducted by NMR (i.e. ¹H) and UV–Vis spectrophotometers. Since the substitution kinetics and DNA/protein interactions were performed in buffer (having water), we evaluated the possibility of H_2O to coordinate to the metal complexes, i.e. the ability of Cl⁻ to be solvated. The binding of the aqua species to the metal centre is known to influence ligand substitution kinetics and electron rate constants [25]. Though the hydrolysis of metal complexes can be determined by NMR spectroscopy, UV–Vis measurements tend to be more suitable, particularly when buffered solutions are employed [26]. The invariant UV–Vis spectra of **PdL₁–PdL₄** (both intensity and position bands) over the 48-h period (Fig. S31), strongly point to the absence
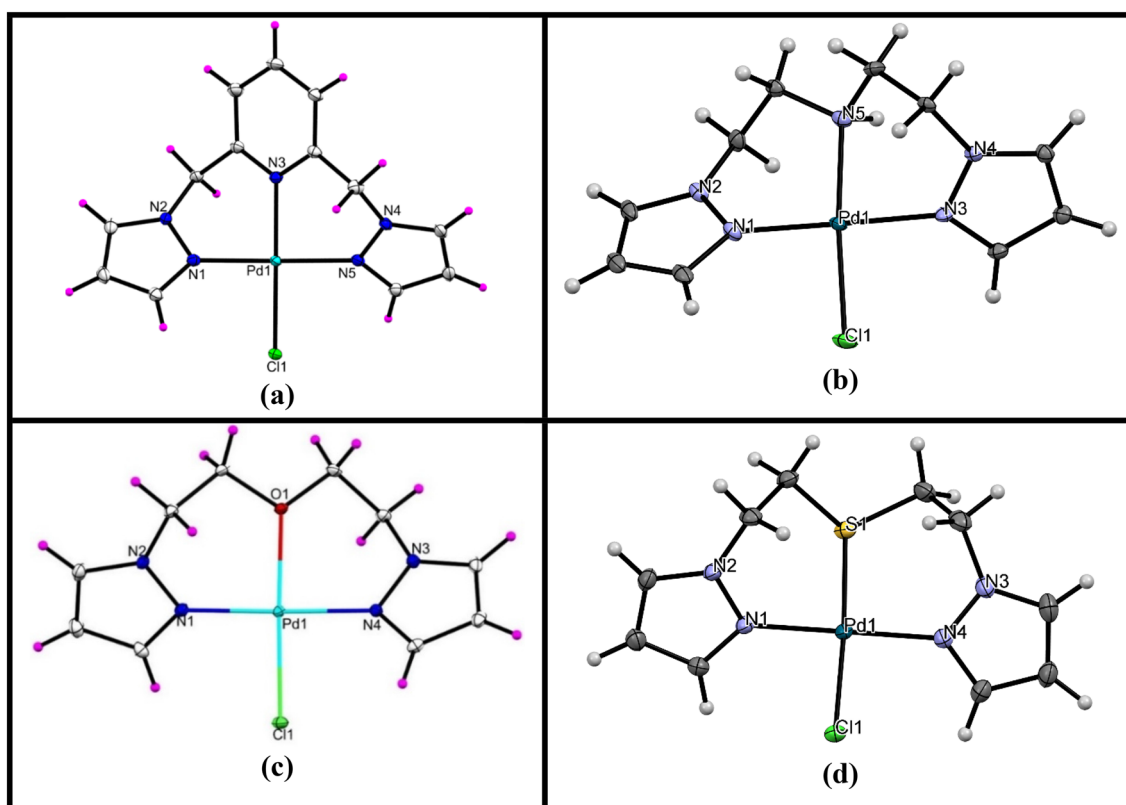

Fig. 1 ORTEP diagram (50% thermal ellipsoids) of **a PdL₁**, **b PdL₂**, **c PdL₃** and **d PdL₄**

of solvent ligand-exchange reactions, hence stability of the compounds in buffer solution.

Often metal complexes undergo ligand dissociation upon dissolution in DMSO stock solutions used in biological assays [27, 28], and thus we studied the effects of DMSO on **PdL₁**–**PdL₄**. No significant changes in the electronic absorption spectral traces were observed within 72 h (Fig. S32), indicative of their stability in DMSO for cellular studies). Furthermore, the ^{1}H NMR spectral data of complexes **PdL₁** (Fig. S33a) and **PdL₄** (Fig. S33b) reveal that DMSO-mediated ligand dissociation did not take place, consistent with the UV–Vis spectra.

Electrochemical properties of palladium(II) PdL₁–PdL₄ complexes

To further gain insight on the electronic structures of **PdL₁**–**PdL₄**, their electrochemical measurements were examined using a combination of cyclic voltammetry (CV) and square wave voltammetry (SWV). Typical CV and SWV voltammograms of **PdL₁**–**PdL₄** are shown in Fig. S34–37, respectively. The wave shapes are very similar for the complexes, displaying irreversible reductive behaviour involving the transfer of two electrons. While the anodic scan of the complexes did not display well-defined oxidation signals, the cathodic runs showed reduction peaks at -1.4 V (**PdL₁**) -1.1 V (**PdL₂**) -0.89 V (**PdL₃**) and -1.1 V (**PdL₄**) (Figs. S35–S38, respectively), indicative of ligand–metal charge transfer reductions [29]. The order of the reduction peaks of the complexes is in accordance with the sequence of the electron-donating effects of the species S (**PdL₄**) > NH (**PdL₂**) and O (**PdL₃**). The reduction values (negative) can be ascribed to high electron cloud on the Pd(II) metal

character, increasing the dπ(Pd) orbital energy as a result of the electron richness of the spectator ligands, leading to a lower energy MLCT absorption. This argument is well supported by the DFT-optimised frontier orbital density distributions (Fig. S38), with the considerable localisation of the LUMOs on the Pd character suggesting the potential σ-donor ability of the spectator ligands. The cathodic wave of **PdL₁** (-1.4 V) is rather unusual because pyridine is a good pi-acceptor. The absence of oxidation waves explicitly signifies the reactive nature of the reduced forms of Pd(II) complexes [29].

Kinetic and mechanistic study

Concentration effect

The kinetics of displacing the chloro ligands with the nucleophiles was studied using stopped-flow instruments by examining the changes in the absorbance of the spectra (at a befitting wavelength) with time, to produce kinetic traces. Noteworthy, the traces generated the observed pseudo-first-order rate constants (k_{obs}) using eqn (S1, SI), indicating that the reactions were first order. The obtained k_{obs} values were plotted on different concentration of the nucleophiles [Nu]. Plots of k_{obs} against [Nu] obtained for **PdL₁**–**PdL₄** at 298 K are given in Fig. S39–S42, respectively. Linear plots of k_{obs} on [Nu] with zero intercept were exhibited in all complexes, suggesting irreversible or non-solvotic pathways. By reducing the positive inductive effect, the reactions can best be described by eqn (S3, SI). The rate constants, k_2 were derived from the gradient of a plot of k_{obs} on [Nu], and the acquired values are provided in Table 1.

Table 1 The rate constants (k_2), activation enthalpy ($\Delta H^{\neq}$) and entropy ($\Delta S^{\neq}$) and Gibbs free energy of activation ($\Delta G^{\neq}$) for the reactions of the complexes with the biological nucleophiles, in aqua solution (50 µM Tris–HCl buffer, containing 50 mM NaCl, pH = 7.2)

Complex	Nu	k_2/M^{-1} s^{-1}	$\Delta H^{\neq}$/ kJ mol^{-1}	-$\Delta S^{\neq}$/Jmol^{-1} K^{-1}	$\Delta G^{\neq}_{25\,°C}$/kJ mol^{-1}
PdL₁	Tu	595 ± 10	14 ± 1	147 ± 3	58 ± 2
	L-Met	218 ± 4	20 ± 1	134 ± 3	60 ± 2
	5'-GMP	54 ± 2	25 ± 1	129 ± 3	63 ± 2
PdL₂	Tu	432 ± 4	15 ± 1	144 ± 3	57 ± 1
	L-Met	186 ± 4	20 ± 1	135 ± 4	60 ± 3
	5'-GMP	30 ± 1	25 ± 1	134 ± 4	65 ± 3
PdL₃	Tu	237 ± 3	24 ± 1	120 ± 3	60 ± 2
	L-Met	105 ± 2	31 ± 1	103 ± 4	62 ± 3
	5'-GMP	13 ± 0.1	34 ± 1	110 ± 3	67 ± 2
PdL₄	Tu	830 ± 10	14 ± 1	141 ± 3	56 ± 2
	L-Met	381 ± 3	22 ± 1	122 ± 3	58 ± 2
	5'-GMP	88 ± 1	22 ± 1	134 ± 3	62 ± 2
PdL₁[a]	Tu	6146 ± 78	27 ± 1	83 ± 3	-
	L-Met	2877 ± 28	30 ± 1	79 ± 3	-
	5'-GMP	927 ± 13	30 ± 1	86 ± 4	-

[a]Data retrieved from ref [18]

The values of rate constant (k_2) of complexes followed the order: $\textbf{PdL}_4 > \textbf{PdL}_2 > \textbf{PdL}_3$ (Table 1). The observed reactivity is associated with the electronic abilities of the auxiliary ligand(s). The higher reactivity of $\textbf{PdL}_4$ (S) in comparison to both $\textbf{PdL}_2$ (NH) and $\textbf{PdL}_3$ (O) is due to the preference of Pd atom (soft acid) to coordinate with the soft donor S atom as opposed to NH and O atom (hard bases), leading to the electron accumulation in the bonding area and, thus, a stronger σ-bonding to the metal centre [30]. The consequence of this is the weak and elongated bond *trans* to the Cl atom, which accelerates reactivity rate [31, 32]. The Pd(1)–Cl(1) bond distances of solid-state structures of 2.293(2), 2.2574(4), and 2.315(6) Å, for $\textbf{PdL}_2$, $\textbf{PdL}_3$ and $\textbf{PdL}_4$ (Table S2) support the argument.

The higher intrinsic reactivity of $\textbf{PdL}_2$ (NH) than $\textbf{PdL}_3$ (O) is due to the better polarizability of NH (with larger and more diffuse electron cloud) compared to O atom. On the rows of the periodic table, polarizability decreases from left to right [33]. Polarisability allows for easy movement of electrons between the heteroatoms and Pd(II) ion (causing a stronger sigma-bond), leading to the elongation of Pd–Cl bond distance. The claims are supported by the shorter X-ray bond distances of Pd(1)–NH of 2.065(7) ($\textbf{PdL}_2$) in comparison to Pd(1)–O of 2.0849(12) Å ($\textbf{PdL}_3$). The solid-state structure Pd(1)–Cl(1) bond length of 2.293(2) Å for $\textbf{PdL}_2$, and 2.2574(4) Å for $\textbf{PdL}_4$ are consistent with the proposition of an increased elongation of Pd–Cl bond. Likewise, the computed bond lengths of Pd-heteroatoms and Pd–Cl for $\textbf{PdL}_2$ and $\textbf{PdL}_3$ (Table S2) are in tandem with the observed kinetic trend. Moreover, the higher polarizability of the heteroatoms in the complexes induces greater dipole moments [34]. The observation agrees well with the computed dipole moments of 15.538 ($\textbf{PdL}_2$) and 14.226 ($\textbf{PdL}_3$), Table S2.

The observed high reactivity of $\textbf{PdL}_1$ in relation to $\textbf{PdL}_2$ can be accounted for both by the electronic and steric influence of the spectator ligand(s). The out-of-square conformations of $\textbf{PdL}_2$ compared to the rigid planar structure of $\textbf{PdL}_1$ introduce steric effects, minimising facile nucleophilic attack. This assertion is evidenced by the X-ray dihedral angle of N(1)–Pd(1)–N(3), 89.81(8) ° ($\textbf{PdL}_1$), which is smaller than N(1)–Pd(1)–N(5), 93.5(3) ° ($\textbf{PdL}_2$). Concerning electronic effects, the pi-acceptor ability of the pyridine moiety ($\textbf{PdL}_1$) reduces electron cloud on the Pd(II) ion, while the NH moiety ($\textbf{PdL}_2$), a good sigma donor, donates electrons to the metal centre [35–37]. The argument is well supported by the DFT computed high positive NBO charge of Pd atom in $\textbf{PdL}_1$ (0.443) in comparison to $\textbf{PdL}_2$ (0.423), Table S3. This is further evidenced by the calculated lower $\Delta E_{\text{LUMO–HOMO}}$ for $\textbf{PdL}_1$ (4.024 eV) than $\textbf{PdL}_2$ (4.128 eV), which makes a metal-to-ligand charge transfer (MLCT) transitions easier ($\textbf{PdL}_1$), Table S3. The ΔE back-donations of 0.503 and 0.516 eV for $\textbf{PdL}_1$ and $\textbf{PdL}_2$, respectively, agree with the observed reactivity trend. Likewise,

the chemical hardness (η), electrophilicity index (ω), and nucleophilicity (ε). The kinetic reactivities of $\textbf{PdL}_1$–$\textbf{PdL}_4$ (with heteroatoms directly coordinated to the Pd(II) ion) are lower than those of our previously published work (heteroatoms non-coordinated to the Pd(II) metal centre [18]. In our earlier work, the reactivities of the complexes are largely influenced by the *pi*-back donation resulting in a more electrophilic Pd(II) metal centre, while in the present study, the k_2 values were influenced by polarizability of the heteroatoms. The rigid and planar nature of the complexes in the previous study also contribute to their enhanced reactivity, while the CH_2 linkers in the current work make the complexes to deviate out of the of plane (as shown by the DFT-planarity diagrams in Fig. S38). The entering ligands **Tu**, **L-Met** and **5'-GMP**, were studied due to their varied electronic and steric demands, binding abilities, and bio-relevance (Chart 1) [38, 39]. Nucleophiles **Tu** and **L-Met** were employed as models for suphur-containing molecules, which are plenty in the blood plasma. The molecule **5'-GMP** (nitrogen donor) was utilised as a representation for nucleobases binding. The reactivities for the incoming ligands follow the order **Tu < L-Met < 5'-GMP** for all complexes. Nucleophiles **Tu** and **L-Met** display greater reactivity to **5'-GMP** owing to the fact that soft acids such as Pd(II) ions (which are very polarizable) prefer to form coordinate bonds with sulphur atom [39]. Among the selected nucleophiles, **Tu** demonstrated the highest reactivity since it is the least voluminous ligand. The slightly greater reactivity of **L-Met** can be explained by the electron releasing nature (positive inductive effect) of the CH_3 substituents that enhances its nucleophilicity. The least reactivity of **5'-GMP** can also be accounted for by its steric bulkiness in comparison to the other two nucleophiles.

Temperature effect and iso-kinetic relationship

To establish $\Delta H^{\neq}$, $\Delta S^{\neq}$ and $\Delta G^{\neq}_{25\,°C}$, k_2 values were examined within the range of 25–45 °C with 5 °C interval. These parameters were determined from the Eyring plots using eqn (S4, SI). Illustrative plots of $\textbf{PdL}_1$–$\textbf{PdL}_4$ with the entering ligands are shown in Figs. S43–S46, respectively. The gradient and intercepts of the plots gave $\Delta H^{\neq}$ and $\Delta S^{\neq}$, respectively, and these values are presented in Table 1. The negative $\Delta S^{\neq}$ values can be attributed to the contribution of the solvent electrostriction that elongates Pd–Cl bond distance in the transition state solvation, increasing the dipole moment of the complexes. Consequently, as shown in Table S3, the dipole moment of $\textbf{PdL}_4$ in the transition state is greater than those of complexes $\textbf{PdL}_2$ and $\textbf{PdL}_3$. The values of $\Delta S^{\neq}$ get more negative with the small size of the entering ligand (**Tu**), and this could be attributed to the constructive overlap between the van der Waals radii, creating a penta-coordinate intermediate with a smaller nucleophile.

The negative $\Delta S^{\neq}$ values indicate an associative mechanism of substitution reaction [40].

Free energy relationships (i.e. linear free energy relationships) was obtained from the plots of $\Delta H^{\neq}$ versus $\Delta S^{\neq}$ using eqn (S5, SI). The straight line of the plots indicated the presence of a linear free energy relationships near iso-kinetic temperature. The slopes of the plots provided the *iso*-kinetic temperature, T_{iso} (an arbitrary temperature at which similar reactions proceed at the same rate), while the intercept gave $\Delta G^{\neq}$. The T_{iso} was obtained at 450.22 K, while $\Delta G^{\neq}$ was computed at 79,695.21 kJ mol^{-1} (Fig. S46b). The magnitude of $\Delta G^{\#}_{25\,°C}$ values (Table 1) are comparable (with $\delta\,\Delta G^{\#}_{25\,°C}$ ~ 0), demonstrating that the substitution reactions proceed through the same mechanism, which is associative [41, 42]. Moreover, the graph shows a near-linear fit with R^2 value of 0.9651, indicating a correlation between $\Delta H^{\neq}$ and $\Delta S^{\neq}$.

DNA interactions studies

Electronic absorption spectroscopic assay

DNA binding properties of **PdL$_1$**–**PdL$_4$** were examined by UV–Vis spectroscopy. The electronic absorption spectral curves for **PdL$_1$**–**PdL$_4$** are provided in **Figs. S47–S50**, respectively. The observed equilibration time for Pd–DNA complexes being less than 30 s. The titration curves show that the addition of DNA results to hypochromism shift in the absorption bands, indicative of the existence of intercalative binding mode [43]. The intrinsic binding constant, K_b, was ascertained utilising eqn (S6, SI), and the free energy (ΔG) of the complex-induced DNA, was quantitatively obtained from eqn (S7, SI), are presented in Table 2. The computed K_b values (ranging from 1.38×10^5 M^{-1} to 5.54×10^5 M^{-1}) compare well with those of related Pd(II) complexes in literature [44–46], and indicate strong binding affinity to DNA helix via intercalative binding mode. The negative values of ΔG demonstrate that the interactions between the Pd complexes and DNA occur spontaneously [47, 48].

EB–DNA competitive measurements

Competitive binding titrations using EB-bound CT-DNA were conducted to further understand the mode of interactions between the metal complexes and DNA. Changes in the fluorescence spectrum of EB–DNA with increasing concentrations of **PdL$_1$**–**PdL$_4$** are presented in Figs. S51–S54, respectively. Considerable decrease in the emission intensity bands at 597 nm was noted with the increasing amounts of individual metal complexes, indicating that Pd- complexes can effectively compete with EB for binding to DNA and thus affirming the intercalation of the complexes to base pairs of DNA [45, 46]. From the spectral data, the Stern–Volmer binding constant (K_{SV}) and the bimolecular quenching rate constant (k_q) were determined from eqn (S8, SI), Stern–Volmer plots and the binding constants values are given in Table 2. The K_{sv} values of (1.10–26.40×10^3 M^{-1}) were 10^4- fold lower than that of the classical intercalator EB (10^7 M^{-1}), indicating that the complexes bind less strongly than EB [49]. The apparent binding ability constant, K_{app}, was derived from eqn (S9, SI). The 10^5–10^6 M^{-1} magnitudes of K_{app} of **PdL$_1$**–**PdL$_4$** are lower than the classical intercalators and metallo-intercalators binding constant (10^7 M^{-1}) [50], affirming moderate intercalating agents to DNA. The k_q values of 9.17×10^{11} M^{-1} s^{-1} for **PdL$_1$**, 6.92×10^{11} M^{-1} s^{-1} for **PdL$_2$**, 4.80×10^{10} M^{-1} s^{-1} for **PdL$_3$**, and 11.49×10^{11} M^{-1} s^{-1} for **PdL$_4$** (Table 2) are greater than the maximal limit of collisional (dynamic) quenching rate constant (2.0×10^{10} M^{-1} s^{-1}), suggesting the presence of static quenching mechanism [51]. The DNA binding constant, K_F values, and the number of binding sites per nucleotide, n, were computed from eqn (S10, SI), and Scatchard plots. The calculated values are provided in Table 2. The values of K_F (magnitude 10^2 or 10^3 M^{-1}) are comparable with those of similar Pd- complexes [45]. The n values are $\approx$ to 1 (Table 2), implying one binding site available in DNA. The order of the calculated competitive binding constants is in tandem with the K_b values and substitution kinetics trend.

Table 2 DNA binding constants derived from the UV–Vis and EB–DNA fluorescence experiments for the Pd complexes

Complex	UV–Vis titration		Fluorescence emission titration				
	K_b (10^5 M^{-1})	$-\Delta G^{\neq}_{25\,°C}$/kJmol^{-1}	K_{sv} (10^4 M^{-1})	K_{app} (10^6 M^{-1})	k_q (10^{11} M^{-1} s^{-1})	K_F (10^3 M^{-1})	n
PdL$_1$	4.99 ± 0.50	32.51	2.11 ± 0.13	10.76 ± 0.77	9.17 ± 0.32	2.17 ± 0.36	0.74
PdL$_2$	3.66 ± 0.41	31.74	0.59 ± 0.02	8.43 ± 0.43	6.92 ± 0.11	1.81 ± 0.01	1.09
PdL$_3$	1.38 ± 0.32	29.32	0.11 ± 0.01	0.80 ± 0.15	0.48 ± 0.02	0.21 ± 0.01	0.79
PdL$_4$	5.54 ± 0.51	32.77	2.64 ± 0.22	14.71 ± 0.91	11.49 ± 0.81	6.00 ± 0.12	0.82
PdL$_1$[a]	55.3	-	5.43 ± 0.21	2.96 ± 0.19	23.6 ± 2.70	1659 ± 13.00	1.34

[a]Data retrieved from ref [18]

Protein-binding studies

Fluorescence quenching measurements

In the current study, BSA was chosen as the model protein due to its high structural similarity with the human serum albumin (HSA), incredible ligand binding abilities, and availability. The fluorescence intensity of tryptophan moiety was examined over the wavelength of 240–320 nm. As shown in Fig. S55 (**PdL₁**), Fig. S56 (**PdL₂**), Fig. S57 (**PdL₃**), and Fig. S58 (**PdL₄**), the addition of metal complexes to BSA solution led to a notable decline in the BSA emission intensity at 281 nm (proving the biding of the complexes with BSA in the hydrophobic cavity of subdomain IIA, i.e. Trp 214). The binding constants, K_{sv} and k_q, were obtained from Stern–Volmer equation. Conversely, K_F and n values were computed from the Scatchard equation and plots. The values of K_{SV}, k_q, K_F, and n are given in Table 3. The K_{SV} values in the order of 10^5 M^{-1} of **PdL₁**–**PdL₄** were much lower than the orders of 10^7 M^{-1} for classical intercalators. This indicated that the process of interaction is not fully controlled by diffusion, but may be assigned to the presence of parallel quenching processes [52]. The obtained k_q values ($> 10^{13}$ M^{-1} s^{-1}), which are greater than those of dynamic quenchers (2.0×10^{10} M^{-1} s^{-1}), demonstrating the presence of a static quenching [53], and a high quenching efficiency of the complexes. The K_F values ($\approx 10^6$ or 10^7 M^{-1}) for **PdL₁**–**PdL₄** are within the ideal range and are high enough to facilitate considerable attachment and transportation of the complexes to the desired target cells [54]. The magnitudes of K_F values ($> 10^5$ M^{-1}) which are high, imply the

interactions of the complexes with the BSA are mainly due to hydrophobic interactions (situated in the subdomain IIA of BSA [55]). The n values of about 1 point to a single-binding site in each albumin. The order of the magnitude of BSA, DNA and competitive binding constants match the kinetic reactivity trends of the complexes (i.e. **PdL₄** > **PdL₂** > **PdL₃** and **PdL₁** > **PdL₂**) and this is attributed to both electronic and steric effects. In general, DNA binding constants are lower than those of our previously related compounds (with the heteroatoms in the cis-positions) [18].

Biomolecular docking simulations

Molecular docking plays a great role in understanding drug–receptor interactions [56]. The compounds **PdL₁**–**PdL₄** were docked into the binding site of DNA as depicted in Figs. S59 and S60. The properties of binding within specific distance and binding energies of the metal complexes are presented in Table 4. The docked energies of the complexes were relatively the same (-12 ± 0.7 kcal/mol), with very favourable best-docked conformation. Complexes **PdL₁**–**PdL₄** exhibited good binding affinities towards DNA. The energy calculation results ranked **PdL₄** as the most energetically favoured interaction with DNA with a MM-GBSA value of -50.59 kcal/mol, while **PdL₁** is least favoured with MM-GBSA value of -41.94 kcal/mol (Table 4). Though **PdL₁**–**PdL₄** are non-planar (as depicted by the planarity diagrams Fig.S38), their docked models (Fig. 2A show intercalative binding mode (proper intercalating gap), in tandem with the experimental measurements.

The interactions of **PdL₁**–**PdL₄** with BSA are shown in Figs.2A and S61. Interactions such as hydrogen bonds, salt bridges, and hydrophobic interactions were observed between BSA residues and atoms of **PdL₁**–**PdL₄**. The simulated docked energies follow the order **PdL₂** (-9.5 kcal/mol) > **PdL₃** (-8.8 kcal/mol) > **PdL₁** (-8.7 kcal/mol) > **PdL₄** (-8.4 kcal/mol). The MM-GBSA energy calculation proved that the compounds were energetically favoured in the order of **PdL₂** (-59.53 kcal/mol) < **PdL₄** (-61.24 kcal/mol) < **PdL₃** (-62.35 kcal/mol) < **PdL₁** (-69.75 kcal/mol), Table S12.

**Table 3** BSA binding constants and parameters for the Pd(II) complexes

Complex	$K_{sv} \times 10^6$, M^{-1}	$k_q \times 10^{13}$, M^{-1} s^{-1}	$K_F \times 10^6$, M^{-1}	n
PdL₁	2.12 ± 0.13	9.22 ± 0.51	6.70 ± 0.11	1.08
PdL₂	2.08 ± 0.24	9.07 ± 0.34	3.24 ± 0.22	1.03
PdL₃	1.35 ± 0.21	5.85 ± 0.33	1.00 ± 0.12	1.17
PdL₄	2.99 ± 0.14	12.98 ± 0.53	40.16 ± 0.66	1.17

Table 4 Interaction properties of complexes: DNA–Pd(II) complexes analysed by XP visualizer and MM-GBSA module

| Complex	Dock score	MM-GBSA	H-bond (Å)	Pi-cation (Å)
DNA–PdL₁	− 12.5	− 41.94	Thymine[7b] (2.24, 2.76)	–
DNA–PdL₂	− 12.7	− 43.42	Thymine[7b] (2.14)	Adenine[6b,9b] (4.27, 4.37, 4.60)
DNA–PdL₃	− 12.3	− 49.33	Thymine[7b] (2.20, 2.22)	Adenine[9b] (3.72, 3.83)
DNA–PdL₄	− 12.6	− 50.95	–	Adenine[6a,6b] (3.29, 4.57)

Superscript numbers indicate the position of the base while letters show the type of strand. Numbers indicated within brackets represent the distance of interacting atoms in Amstrong (Å). The more negative binding free energy, the stronger the binding affinity between DNA and **PdL₁**–**PdL₄**. Generally, the lower relative binding energies of the complexes could be ascribed to their non-planar nature (as shown in DFT computations, Fig. S38)
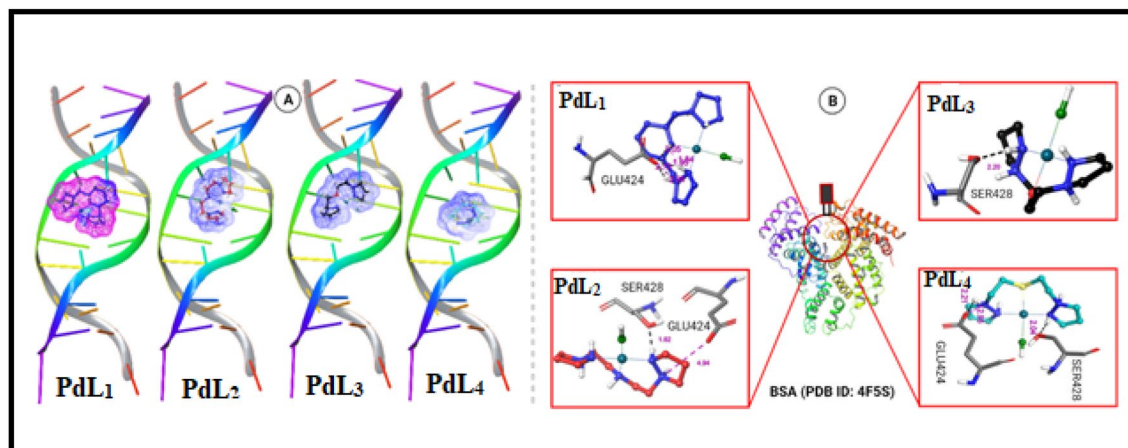
Fig. 2 A Docked poses of DNA–**PdL$_{1-4}$** interactions, indicating intercalative mode of action corroborating the experimental results. **B** 3D Interaction diagrams of **PdL$_1$**–**PdL$_4$** with BSA 3D. Black dotted line represents hydrogen bond while pink dotted lines represent salt bridge interaction
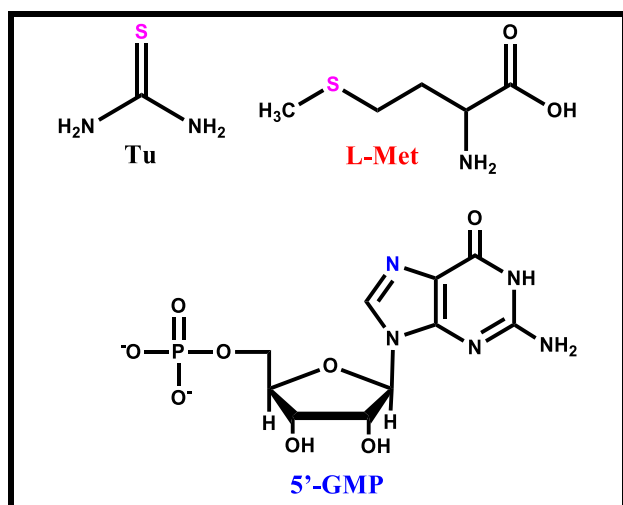
Chart 3 Structures of the investigated biological donor nucleophiles

In vitro cytotoxicity assay

We next addressed the cytotoxicity of **PdL$_1$–PdL$_4$** against two cell lines—the human cervical adenocarcinoma (HeLa) and the transformed (immortalised) human lung fibroblast (MRC-5 SV2) cell lines, with cisplatin as the reference anticancer drug, employing the MTT assay protocol. The cells were exposed to concentrations up to 100 μM for 48 h, and the resultant viability data are shown in Fig. S62. The standard drug, cisplatin, reduced cell viability significantly in a concentration-dependent manner, with IC$_{50}$ values below 20 μM and 35 μM for the HeLa and MRC-5 SV2 cells, respectively (Table 5). However, despite having reasonable DNA/BSA interactive capabilities (Tables 2 and 3), **PdL$_1$–PdL$_4$** were not quite active (cytotoxic) against the

Table 5 IC$_{50}$ values for the effects of the Pd(II) complexes against Hela and MRC-5 SV2 cell lines

Cell line	IC$_{50}$ (μM)				
	PdL1	PdL2	PdL3	PdL4	Cisplatin
HeLa	> 100	> 100	> 100	> 100	19.3 ± 0.4
MRC-5 SV2	> 100	> 100	> 100	> 100	31.1 ± 6.4

Note: Values are Mean $\pm$ SEM (n = 3). The compound cisplatin was used as a positive control (based on the MTT assay)

two cell lines (IC$_{50}$ values > 100 μM), Table 5. This low cytotoxicity may be attributed to the presence of the methylene linkers, which reduces the aromaticity and planarity of the spectator ligands [57–59]. In addition, the relatively low kinetic reactivity of the complexes ($k_2 \sim$ magnitude 10^2) could account for their lower cytotoxic effects, since some degree of kinetic reactivity is required for the drug to reach the DNA target [60]. From our previous studies Pd(II) complexes with k_2 values ranging from 10^3 to 10^4 displayed better cytotoxic potency comparable to cisplatin [18, 61].

Conclusions

In this current work, a set of Pd(II) complexes bearing pyrazol-1-yl ligands have been successfully prepared and structurally characterised by numerous spectroscopic techniques. The crystal structures of the studied complexes showed square-planar coordination geometry. The electrochemical studies of **PdL$_1$–PdL$_4$** reveal irreversible, two-electron reduction reactions. The substitution kinetics of the complexes are associated to the *trans*-effects of the atoms on the carrier ligand(s), with **PdL$_4$** displaying the highest kinetic

reactivity, while **PdL₃** demonstrates the lowest reactivity. The trend of kinetic reactivity was substantiated by DFT results. The values of activation parameters for **PdL₁–PdL₄** ($\Delta H^{\neq} > 0$, $\Delta S^{\neq} < 0$) signify associative mechanism for the substitution process. The examined complexes have strong affinity towards DNA through a non-covalent binding known as intercalative mode, consistent with the bio-molecular simulations. BSA binding parameters conclude reasonable binding of the complexes to protein, suggesting that BSA can act as a carrier protein for the complexes. MM-GBSA energy calculations reveal good binding strength of the complexes to BSA. However, the complexes displayed minimal in vitro cytotoxicity (with IC_{50} values > 100 μM), highlighting the fact that effective DNA/BSA of metal complexes alone is not enough to guarantee cytotoxicity.

Experimental section

Preparation and characterisation of Pd(II) complexes

[{2,6-bis((1H-pyrazol-1-yl)methyl)pyridine]PdCl}]BF₄ (PdL₁). Ligand **L₁** (0.10 g, 0.39 mmol) was added to a solution of [PdCl₂(NCMe)]₂ (0.10 g, 0.39 mmol) and NaBF₄ (0.04, 0.39 mmol) in CH_2Cl_2 (30 mL) to afford a yellow solution. The mixture was stirred for 12 h and filtered to remove the precipitate of NaCl through a short pad. To the filtrate Et_2O (10 mL) was added to obtain **PdL₁** as a yellow solid. Single-crystals of **PdL₁** were obtained by allowing Et_2O to diffuse into concentrated solution of CH_2Cl_2. Yield: 1.1 g (60%). ¹H NMR (400 MHz, DMSO-d₆): δ_H (ppm): 6.10 (s, 4H, CH₂); 6.63 (t, $^3J_{HH} = 3.3$, 2H, pz); 7.92 (dd, $^3J_{HH} = 3.3$, 2H, pz); 7.95 (d, $^3J_{HH} = 7.8$, 2H, pz); 8.30 (dd, $^3J_{HH} = 3.3$, 2H, py); 8.37 (t, $^3J_{HH} = 7.8$, 2H, py). ¹³C NMR (DMSO-d₆): δC (ppm): 60.13; 107.8; 121.42; 137.21; 139.01; 148.11; 156.85. FT-IR (cm⁻¹): υ(C–H) = 3080; υ(C=C) = 1510; υ(C=N) = 1415; υ(C–N) = 1071. TOF MS/ES⁺, m/z (%) 381 (M⁺, 100). Anal. Calcd. (%) for C₁₃H₁₃BClF₄N₅Pd: C, 33.37; H, 2.80; N, 14.97. Found (%): C, 33.63; H, 2.58; N, 15.17.

Complexes **PdL₂–PdL₄** were prepared based on the same synthetic method described for **PdL₁.**

[{bis[2-(1H-pyrazol-1-yl)ethyl]amine}PdCl]BF₄ (PdL₂): **L₂** (0.16 g, 0.78 mmol), [PdCl₂(CH₃CN)₂] (0.20 g, 0.78 mmol) and NaBF₄ (0.08 g, 0.78 mmol). Yellow solid. Crystals for **PdL₂** were attained from slow evaporations of concentrated CH_2Cl_2 solutions. Yield: 0.28 g (83%). ¹H NMR (400 MHz, DMSO-d₆): δ_H (ppm): 2.97–3.03 (m, 4H, CH₂); 4.54–4.60 (m, 2H, CH₂); 4.82–4.89 (m, 2H, CH₂); 6.54 (t, $^3J_{HH} = 2.0$, 2H, pz); 7.13 (s, 1H, NH); 8.00 (dd, $^3J_{HH} = 2.0$, 2H, pz); 8.15 (d, $^3J_{HH} = 2.0$, 2H, pz). ¹³C NMR (DMSO-d₆): δC (ppm): 49.50; 49.89; 106.94; 134.99; 143.05. FT-IR

(cm⁻¹): υ(C–H) = 3096; υ(C=C) = 1520; υ(C=N) = 1408; υ(C–N) = 1035. LC MS/ESI⁺, m/z (%) = 346 [M⁺, 100]; 692 [M⁺, 10]. Anal. Calcd. (%) for C₁₀H₁₅BClF₄N₅Pd: C, 27.68; H, 3.48; N, 16.14. Found (%): C, 27.44; H, 3.78; N, 15.80.

[{bis-2-(1H-pyrazol-1-yl)ethyl]ether}PdCl]BF₄ (PdL₃): **L₃** (0.16 g, 0.78 mmol), [PdCl₂(CH₃CN)₂] (0.20 g, 0.78 mmol) and NaBF₄ (0.08 g, 0.78 mmol). Single-crystals were obtained by slow evaporation of Et_2O into saturated CH_2Cl_2 solutions. Yield: 0.29 g (85%). ¹H NMR (400 MHz, DMSO-d₆): δ_H (ppm): 3.51 (d, $^3J_{HH} = 10.0$, 2H, CH₂); 4.24 (t, $^3J_{HH} = 10.0$, 2H, CH₂); 4.59 (d, $^3J_{HH} = 12.1$, 1H, CH); 4.71 (d, $^3J_{HH} = 10.0$, 2H, CH₂); 4.99 (t, $^3J_{HH} = 12.1$, 1H, CH); 6.51 (t, $^3J_{HH} = 2.4$, 1H, pz); 6.58 (t, $^3J_{HH} = 2.4$, 1H, pz); 8.06 (d, $^3J_{HH} = 2.3$, 1H, pz); 8.12 (d, $^3J_{HH} = 2.3$, 1H, pz); 8.20 (d, $^3J_{HH} = 2.0$, 1H, pz); 8.57 (d, $^3J_{HH} = 2.0$, 1H, pz). ¹³C NMR (DMSO-d₆): δC (ppm): 51.61; 52.30; 69.58; 70.13; 107.07; 107.66; 135.43; 136.66; 141.37; 142.43. FT-IR (cm⁻¹): υ(C–H) = 3107; υ(C=C) = 1511; υ(C=N) = 1412; υ(C–O) = 1275; υ(C–N) = 1049. LC MS/ESI⁺, m/z (%) = 347 [M⁺, 100]. Anal. Calcd (%) for C₁₀H₁₄BClF₄N₄OPd: C, 27.62; H, 3.24; N, 12.88; O, 3.68. Found (%): C, 27.43; H, 3.16; N, 12.49; O, 3.82.

[{bis[2-(1H-pyrazol-1-yl)ethyl]sulphide}PdCl]BF₄ (PdL₄). **L₄** (0.17 g, 0.78 mmol), [PdCl₂(NCMe)]₂ (0.20 g, 0.78 mmol) and NaBF₄ (0.08 g, 0.78 mmol). Yellow solid. Single-crystals were acquired by the diffusion of Et_2O into CH_2Cl_2 solution. Yield: 0.3 g (85%). ¹H NMR (400 MHz, DMSO-d₆): δ_H (ppm): 3.36 (d, $^3J_{HH} = 2.8$, 2H, CH₂); 3.63 (q, $^3J_{HH} = 2.8$, 2H, CH₂); 5.06 -5.11 (m, 2H, CH₂); 5.24– 5.31 (m, 2H, CH₂); 6.58 (t, $^3J_{HH} = 2.0$, 2H, pz); 8.01 (d, $^3J_{HH} = 2.0$, 2H, pz); 8.19 (d, $^3J_{HH} = 2.0$, 2H, pz). ¹³C NMR (DMSO-d₆): δC (ppm): 36.14 (CH₂); 52.31; 107.63; 135.99; 144.03. FT-IR (cm⁻¹): υ(C–H) = 3142; υ(C=C) = 1515; υ(C=N) = 1415; υ(C–N) = 1058; υ(C–S) = 776. LC MS/ ESI⁺, m/z (%) = 364 [M⁺, 100]. Anal. Calcd (%) for C₁₀H₁₄BClF₄N₄PdS: C, 26.63; H, 3.13; N, 12.42; S, 7.11. Found (%): C, 26.94; H, 2.87; N, 12.57; S, 7.39.

Supplementary information

Experimental procedures and analytical data for the compounds (NMR and FT-IR spectroscopic spectral data, mass spectral, and X-ray crystallography data and files) and biological graphs and Tables are contained in the supporting information. The crystallographic data entries are deposition numbers: 2107406–2107409 for **PdL₁–PdL₄**, respectively.

Declarations

Conflict of interest The authors declare no conflict of interest.

References

1. Joksimović N, Janković N, Petronijević J, Baskić D, Popovic S, Todorović D, Zarić M, Klisurić O, Vraneš M, Tot A (2020) Med Chem 16:78–92
2. Wei X, Yang Y, Ge J, Lin X, Liu D, Wang S, Zhang J, Zhou G, Li S (2020) J Inorg Biochem 202:110857
3. Franich AA, Živković MD, Ćоćić D, Petrović B, Milovanović M, Arsenijević A, Milovanović J, Arsenijević D, Stojanović B, Djuran MI (2019) J Biol Inorg Chem 24:1009–1022
4. Lima MA, Costa VA, Franco MA, de Oliveira GP, Deflon VM, Rocha FV (2020) Inorg Chem Commun 112:107708
5. Divsalar A, Saboury AA, Mansoori-Torshizi H, Ahmad F (2010) J Phys Chem B 114:3639–3647
6. Jahromi EZ, Divsalar A, Saboury AA, Khaleghizadeh S, Mansouri-Torshizi H, Kostova I (2016) J Iran Chem Soc 13:967–989
7. Darabi F, Hadadzadeh H, Simpson J, Shahpiri A (2016) New J Chem 40:9081–9097
8. Churusova SG, Aleksanyan DV, Rybalkina EY, Susova OY, Brunova VV, Aysin RR, Nelyubina YV, Peregudov AS, Gutsul EI, Klemenkova ZS (2017) Inorg Chem 56:9834–9850
9. Muralisankar M, Basheer SM, Haribabu J, Bhuvanesh NS, Karvembu R, Sreekanth A (2017) Inorg Chim Acta 466:61–70
10. Fong TTH, Lok CN, Chung CYS, Fung YME, Chow PK, Wan PK, Che CM (1939) Angew Chem Int Ed 55(2016):11935–11941
11. Ž.D. Bugarčić, G. Liehr, R. van Eldik, J. Chem. Soc., Dalton Trans. (2002) 951–956.
12. Bogojeski J, Jelić R, Petrović D, Herdtweck E, Jones PG, Tamm M, Bugarčić ŽD (2011) Dalton Trans 40:6515–6523
13. Bugarčić ŽD, Petrović B, Zangrando E (2004) Inorg Chim Acta 357:2650–2656
14. Soldatović T, Shoukry M, Puchta R, Bugarčić ŽD, van Eldik R (2009) Eur J Inorg Chem 2009:2261–2270
15. D. Jaganyi, F. Tiba, O.Q. Munro, B. Petrović, Ž.D. Bugarčić, Dalton Trans. (2006) 2943–2949.
16. D.O. Onunga, D. Jaganyi, A. Mambanda, J Coord Chem. (2019) 1–17.
17. Ćоćić D, Jovanović S, Radisavljević S, Korzekwa J, Scheurer A, Puchta R, Baskić D, Todorović D, Popović S, Matić S (2018) J Inorg Biochem 189:91–102
18. R.O. Omondi, R. Bellam, S.O. Ojwach, D. Jaganyi, A.A. Fatokun, J. Inorg. Biochem. (2020) 111156.
19. Sorrell TN, Malachowski MR (1983) Inorg Chem 22:1883–1887
20. García-Antón J, Pons J, Solans X, Font-Bardia M, Ros J (2003) Eur J Inorg Chem 2003:3952–3957
21. Ojwach SO, Guzei IA, Darkwa J, Mapolie SF (2007) Polyhedron 26:851–861
22. A.S. Potapov, E.A. Nudnova, G.A. Domina, L.N. Kirpotina, M.T. Quinn, A.I. Khlebnikov, I.A. Schepetkin, Dalton Trans. (2009) 4488–4498.
23. Cooper SRI (2020) CrystEngComm 22:7186
24. Allen FH (2002) Crystallogr B58:380
25. Zhao J, Xu Z, Lin J, Gou S (2017) Inorg Chem 56:9851–9859
26. Tan C, Liu J, Li H, Zheng W, Shi S, Chen L, Ji L (2008) J Inorg Biochem 102:347–358
27. Hall MD, Telma KA, Chang K-E, Lee TD, Madigan JP, Lloyd JR, Goldlust IS, Hoeschele JD, Gottesman MM (2014) Cancer Res 74:3913–3922
28. Moon S, Hanif M, Kubanik M, Holtkamp H, Söhnel T, Jamieson SM, Hartinger CG (2015) ChemPlusChem 80:231–236
29. Shabbir M, Akhter Z, Ahmad I, Ahmed S, Shafiq M, Mirza B, McKee V, Munawar KS, Ashraf AR (2016) J Mol Struct 1118:250–258
30. Brinck T, Borrfors AN (2019) J Mol Model 25:125
31. Nkabinde SV, Kinunda G, Jaganyi D (2017) Inorg Chim Acta 466:298–307
32. Pitteri B, Bortoluzzi M, Marangoni G (2005) Transition Met Chem 30:1008–1013
33. Miller TM, Bederson B (1978) Adv At Mol Opt Phys 13:1–55
34. Ghahremanpour MM, van Maaren PJ, Caleman C, Hutchison GR, Van der Spoel D (2018) J Chem Theory Comput 14:5553–5566
35. Kosović M, Jovanović S, Bogdanović GA, Giester G, Jaćimović Ž, Bugarčić ŽD, Petrović B (2016) J Coord Chem 69:2819–2831
36. Kosović M, Jaćimović Ž, Bugarčić ŽD, Petrović B (2015) J Coord Chem 68:3003–3012
37. Jaganyi D, Hofmann A, van Eldik R (2001) Angew Chem Int Ed 40:1680–1683
38. Ćоćić D, Jovanović S, Nišavić M, Baskić D, Todorović D, Popović S, Bugarčić ŽD, Petrović B (2017) J Inorg Biochem 175:67–79
39. Jovanović S, Obrenčević K, Bugarčić ŽD, Popović I, Žakula J, Petrović B (2016) Dalton Trans 45:12444–12457
40. J.D. Atwood Journal (1997). *Inorganic and organometallic reaction mechanisms*. John Wiley & Sons
41. Bellam R, Jaganyi D, Mambanda A, Robinson R (2018) New J Chem 42:12557–12569
42. Bellam R, Jaganyi D, Mambanda A, Robinson R, BalaKumaran MD (1894) RSC Adv 9(2019):31877–31883
43. Zhou X-Q, Sun Q, Jiang L, Li S-T, Gu W, Tian J-L, Liu X, Yan S-P (2015) Dalton Trans 44:9516–9527
44. Vuradi RK, Dandu K, Yata PK, Mallepally RR, Chintakuntla N, Ch R, Thakur SS, Rao CM, Satyanarayana S (2018) New J Chem 42:846–859
45. Omondi RO, Bellam R, Ojwach SO, Jaganyi D, Fatokun AA (2020) J Inorg Biochem 210:111156
46. Onunga DO, Bellam R, Mutua GK, Sitati M, BalaKumaran MD, Jaganyi D, Mambanda A (2020) J Inorg Biochem 213:111261
47. Mukherjee S, Mitra I, Fouzder C, Mukherjee S, Ghosh S, Chatterji U, Moi SC (2017) J Mol Liq 247:126–140
48. Karami K, Alinaghi M, Amirghofran Z, Lipkowski J (2018) Inorg Chim Acta 471:797–807
49. İnci D, Aydın R, Zorlu Y (2021) Eur Biophys J 50:771–785
50. Cory M, McKee DD, Kagan J, Henry D, Miller JA (1985) J Am Chem Soc 107:2528–2536
51. Mitra I, Mukherjee S, Misini B, Das P, Dasgupta S, Linert W, Moi SC (2018) New J Chem 42:2574–2589
52. Milutinović MM, Rilak A, Bratsos I, Klisurić O, Vraneš M, Gligorijević N, Radulović S, Bugarčić ŽD (2017) J Inorg Biochem 169:1–12
53. Poloni DM, Dangles O, Vinson JA (2019) J Agric Food Chem 67:9139–9147
54. Fetzer L, Boff B, Ali M, Xiangjun M, Collin J-P, Sirlin C, Gaiddon C, Pfeffer M (2011) Dalton Trans 40:8869–8878

55. Cheng Z-J, Zhao H-M, Xu Q-Y, Liu R (2013) J Pharm Anal 3:257–269
56. Schmidt C, Robinson CV (2014) FEBS J 281:1950–1964
57. Zhou X-Q, Li Y, Zhang D-Y, Nie Y, Li Z-J, Gu W, Liu X, Tian J-L, Yan S-P (2016) Eur J Med Chem 114:244–256
58. G. Ayyannan, M. Mohanraj, M. Gopiraman, R. Uthayamalar, G. Raja, N. Bhuvanesh, R. Nandhakumar, C. Jayabalakrishnan, Inorg. Chim. Acta. (2020) 119868.
59. Karami K, Hosseini-Kharat M, Sadeghi-Aliabadi H, Lipkowski J, Mirian M (2014) Eur J Med Chem 73:8–17
60. R.O. Omondi, S.O. Ojwach, D. Jaganyi, Inorg. Chim. Acta. (2020) 119883.
61. R.O. Omondi, N.R. Sibuyi, A.O. Fadaka, M. Meyer, D. Jaganyi, S.O. Ojwach, Dalton Trans. (2021).

Authors and Affiliations

Reinner O. Omondi[1,2] · **Adewale O. Fadaka**[3,4] · **Amos A. Fatokun**[5] · **Deogratius Jaganyi**[6,7] · **Stephen O. Ojwach**[1]

✉ Stephen O. Ojwach
ojwach@ukzn.ac.za

1 School of Chemistry and Physics, University of KwaZulu-Natal, Private Bag X01, Scottsville, Pietermaritzburg 3209, South Africa

2 Present Address: Department of Chemistry, University of Cape Town, Rondebosch 7701, South Africa

3 Department of Biotechnology, University of the Western Cape, Private Bag X17, Bellville, Cape Town 7535, South Africa

4 Department of Anesthesia, Division of Pain Management, Cincinnati Children's Hospital, Medical Center, Burnet 3322, Avenue, Cincinnati, OH 45229, USA

5 Centre for Natural Products Discovery (CNPD), School of Pharmacy and Biomolecular Sciences, Faculty of Science, Liverpool John Moores University, Liverpool L3 3AF, UK

6 School of Pure and Applied Sciences, Mount Kenya University, P.O. Box 342-01000, Thika, Kenya

7 Department of Chemistry, Faculty of Applied Sciences, Durban University of Technology, P.O. Box 1334, Durban 4000, South Africa